

# The $\Omega(2380)$ as a partner of the $\Omega(2012)$

Yi-Yao Li<sup>1, 2, 3, 4, \*</sup> Albert Feijoo<sup>5, †</sup> and Eulogio Oset<sup>4, 6, ‡</sup>

<sup>1</sup>*State Key Laboratory of Nuclear Physics and Technology, Institute of Quantum Matter,  
South China Normal University, Guangzhou 510006, China*

<sup>2</sup>*Key Laboratory of Atomic and Subatomic Structure and Quantum Control (MOE),  
Guangdong-Hong Kong Joint Laboratory of Quantum Matter, Guangzhou 510006, China*

<sup>3</sup>*Guangdong Basic Research Center of Excellence for  
Structure and Fundamental Interactions of Matter,  
Guangdong Provincial Key Laboratory of Nuclear Science, Guangzhou 510006, China*

<sup>4</sup>*Departamento de Física Teórica and IFIC,  
Centro Mixto Universidad de Valencia-CSIC,  
Institutos de Investigación de Paterna, 46071 Valencia, Spain*

<sup>5</sup>*Instituto de Física Corpuscular, Centro Mixto Universidad de Valencia-CSIC,  
Institutos de Investigación de Paterna,  
Aptdo. 22085, 46071 Valencia, Spain*

<sup>6</sup>*Department of Physics, Guangxi Normal University, Guilin 541004, China*

## Abstract

We present a study of the  $\Omega(2380)$  resonance and show that it is consistent with a dynamically generated state arising from the  $\bar{K}^*\Xi^*$ ,  $\omega\Omega$ , and  $\phi\Omega$  interactions. In this picture, the  $\Omega(2380)$  is analogous to the  $\Omega(2012)$ , which is generated from the  $\bar{K}\Xi^*$  and  $\eta\Omega$  channels. The resulting mass, total width, and partial decay widths into the  $\bar{K}\Xi^*$  and  $\bar{K}^*\Xi$  channels are compatible with the available experimental data. We also discuss possible experimental observables that could provide further insight into the nature of this state.

## I. INTRODUCTION

The spectroscopy of excited  $\Omega^*$  baryons has long remained poorly explored experimentally. For nearly four decades, only three states, i.e.  $\Omega(2250)$ ,  $\Omega(2380)$  and  $\Omega(2470)$ , with two- or three-star status were listed in the Review of Particle Physics (RPP) [1]. This limited experimental information stood in stark contrast to a wide range of theoretical studies based on quark models, Skyrme-type approaches, and lattice QCD (LQCD), which anticipated a significantly richer  $\Omega^*$  spectrum [2–12].

A major breakthrough came with the observation of a narrow resonance, the  $\Omega(2012)^-$ , by the Belle Collaboration in  $e^+e^-$  collisions [13]. The state was reconstructed in the  $K_S^0\Xi^-$  and  $K^-\Xi^0$  decay channels and exhibited a width of about 6 MeV. Comparisons with LQCD calculations [11] and conventional quark-model (CQM) predictions [2–5, 10] favored a spin-parity assignment of  $J^P = 3/2^-$ , consistent with a  $d$ -wave decay, whereas an  $s$ -wave  $J^P = 1/2^-$  assignment would imply a substantially larger width. Subsequent Belle analyses [14, 15] refined the decay properties of the  $\Omega(2012)^-$  and provided a precise determination of the branching-fraction ratio  $\mathcal{R}_{\Xi\bar{K}}^{\Xi\bar{K}\pi}$  [15], which serves as a stringent constraint on theoretical interpretations. Independent evidence for  $\Omega(2012)^-$  production was later reported by the BESIII Collaboration in the process  $e^+e^- \rightarrow \Omega(2012)^-\bar{\Omega}^+ + c.c.$ , together with indications of a new structure, the  $\Omega(2109)^-$  [16]. More recently, the ALICE Collaboration observed a pronounced signal near 2013 MeV in the  $K_S^0\Xi^-$  invariant-mass distribution in  $pp$  collisions at  $\sqrt{s} = 13$  TeV, providing a third independent confirmation of the  $\Omega(2012)^-$  resonance [17].

---

\* [liiyao@m.scnu.edu.cn](mailto:liiyao@m.scnu.edu.cn)

† [edfeijoo@ific.uv.es](mailto:edfeijoo@ific.uv.es)

‡ [eulogio.oset@ific.uv.es](mailto:eulogio.oset@ific.uv.es)

Beyond establishing its existence, these results provide a valuable benchmark for testing theoretical approaches to excited  $\Omega$  states, particularly those based on unitarized meson–baryon dynamics.

The growing body of experimental information has triggered extensive theoretical investigations into the nature of the  $\Omega(2012)^-$ . Numerous studies based on constituent quark models interpret the state as a  $p$ -wave excited baryon [18–28]. In contrast, alternative approaches emphasize the proximity of the  $\Omega(2012)^-$  mass to the  $\bar{K}\Xi(1530)$  threshold and describe it as a dynamically generated hadronic molecule within coupled-channel frameworks [29–40]. It is worth noting that the revised Belle measurement of the branching-fraction ratio [15] provides strong support for the molecular interpretation.

The use of unitarized effective theories (UEFTs) in coupled channels to describe meson–baryon interactions in the strangeness  $S = -3$  sector dates back more than two decades. The dynamical generation of  $S = -3$  baryon resonances from systems composed of pseudoscalar mesons and ground-state decuplet baryons ( $J^P = 3/2^+$ ) was investigated in Refs. [41–43]. In addition, the  $\bar{K}\Xi$  interaction was studied within an extended chiral  $SU(3)$  quark model by solving a resonating group method equation in Ref. [44]. More recently, the exploratory study of Ref. [45] examined the possibility of generating  $\Omega^*$  or  $P_{sss}$  (pentaquark) states from the  $\bar{K}\Xi$  interaction through attractive next-to-leading-order corrections to the chiral Lagrangian. A particularly relevant contribution in this theoretical context is Ref. [46], where a consistent  $SU(6)$  extension of the meson–baryon chiral Lagrangian is implemented within a coupled-channel unitary approach. In that work, a wide set of meson–baryon channels is considered, including all possible combinations of pseudoscalar and vector mesons with ground-state octet and decuplet baryons. As a result, nine  $\Omega^*$  resonances are predicted, two of which are compatible with the experimentally observed  $\Omega(2250)$  and  $\Omega(2380)$ . However, the state associated with the  $\Omega(2380)$  resonance in that work appears as a bound state with a mass of about 1930 MeV, predominantly coupling to the  $\bar{K}\Xi^*$ ,  $\bar{K}^*\Xi$ , and  $\eta\Omega$  channels, and with non-negligible couplings to  $\bar{K}^*\Xi^*$  and  $\phi\Omega$ . Such a low mass automatically precludes its decay into the  $\bar{K}\Xi^*$  and  $\bar{K}^*\Xi$  channels, thereby conflicting with the experimental information on the  $\Omega(2380)$  resonance [47]. This sizable mass discrepancy highlights a persistent difficulty of current coupled-channel approaches including vector mesons and decuplet baryons in accommodating the  $\Omega(2380)$  within a realistic dynamical framework.

Despite these advances, a unified description of the  $\Omega(2380)$  resonance within unita-

ritized effective field theories remains unresolved. In particular, existing coupled-channel approaches either predict states significantly below the experimental mass or fail to reproduce simultaneously the observed decay modes and the sizable width of the  $\Omega(2380)$ , indicating that its dominant dynamical components are still poorly understood. It remains unclear which combinations of vector-decuplet and other meson–baryon channels might generate the observed resonance properties, motivating a detailed investigation in the present work.

In this context, in Ref. [48], the interaction between the vector-meson octet and the baryon decuplet was investigated using Lagrangians derived from the local hidden gauge symmetry approach. In that study, the unitary coupled-channel amplitudes in the  $S = -3$ ,  $I = 0$  sector develop a pole that the authors associated with the  $\Omega(2470)$  resonance, given the proximity between the predicted mass of the state (2449 MeV) and the experimentally reported value. Although this assignment is plausible due to the absence of mixing with lighter channels—which would be expected to increase the width of the state—it nonetheless exhibits a significant discrepancy between the predicted and experimental widths, with the latter being approximately an order of magnitude larger than the theoretical estimate.

Interestingly, both the quark model developed in Ref. [11] and the lattice-QCD-based studies of Refs. [12] indicate a direct association between pure  $|sss\rangle$  configurations and the experimentally observed  $\Omega(2470)$  state, while no clear three-quark configuration can be identified with the  $\Omega(2380)$  resonance. This pattern has been largely sustained in subsequent theoretical investigations. This absence of a clear three-quark counterpart for the  $\Omega(2380)$  strongly suggests that non- $sss$  components may play a dominant role in its structure.

Bearing in mind the elusive  $|sss\rangle$  nature of the  $\Omega(2380)$ , the proximity of the  $\bar{K}^*\Xi^*$  threshold to its mass, and the success of the molecular approach in identifying the dominant meson–baryon nature of the  $\Omega(2012)$  state, it is timely to reexamine the theoretical  $\Omega$ -spectrum within the framework of unitarized effective field theories. In particular, this motivates a renewed study of the interaction between vector mesons and the baryon members of the decuplet. Though within the framework of the quark delocalization color screening model, the interaction between  $\Omega$  baryon and  $s\bar{s}$  mesons (i.e.  $\phi$  and  $\eta'$ ) has been addressed very recently [49], and although the  $\Omega\phi$  interaction in the  $J^P = 1/2^-$  component was found to be attractive, the corresponding strength was not sufficient to bind the system or generate a resonant state.

In the present work, to assess the molecular nature of the  $\Omega(2380)$  resonance, we revisit

the vector meson-decuplet baryon interaction following Ref. [48], with the explicit inclusion of the  $\Xi(1530)^0 K^-$  and  $\Xi^- \bar{K}^{*0}$  channels via box diagrams—corresponding to the only experimentally observed two-body decay modes of the  $\Omega(2380)$ . This allows for a more phenomenologically consistent estimation of the resonance width.

## II. FORMALISM

The work of Ref. [31] studied the  $\Omega(2012)$  state in the  $\bar{K}\Xi^*$ ,  $\eta\Omega$  coupled channels, with  $\bar{K}\Xi$  as the main decay mode. But in the present work, we turn to vector meson-decuplet baryon sector to study the interaction and the possible generation of bound states. The corresponding channels are  $\bar{K}^*\Xi^*(1530)$ ,  $\omega\Omega$ ,  $\phi\Omega$ .

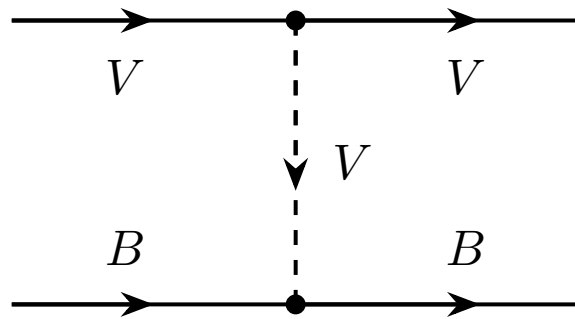


FIG. 1. Diagrammatic representation of the  $VB \rightarrow VB$  interaction, through the exchange of vector meson.

Fig. 1 depicts the interaction of meson-baryon via vector meson exchange following the local hidden gauge approach. The upper  $VVV$  vertex is driven by the Lagrangian [50–53]:

$$\mathcal{L}_{VVV} = ig \langle (V^\mu \partial_\nu V_\mu - \partial_\nu V^\mu V_\mu) V^\nu \rangle, \quad (1)$$

with the coupling constant  $g = \frac{m_V}{2f_\pi}$ , where  $m_V = 800$  MeV is an averaged vector meson mass and  $f_\pi = 93$  MeV is the pion decay constant. The vector meson matrix  $V$  is defined as

$$V = \begin{pmatrix} \frac{\rho^0}{\sqrt{2}} + \frac{\omega}{\sqrt{2}} & \rho^+ & K^{*+} \\ \rho^- & -\frac{\rho^0}{\sqrt{2}} + \frac{\omega}{\sqrt{2}} & K^{*0} \\ K^{*-} & \bar{K}^{*0} & \phi \end{pmatrix}. \quad (2)$$

The Lagrangian of Eq. (1) for  $VB$  close to threshold, neglecting the three momenta of the vectors versus their mass, requires  $\nu = 0$ . For the lower vertex, the  $VBB$  one, we calculate it using an analogous approach to Refs. [54–56]. The vertex is given in terms of quarks and sandwiched between the baryon quark wave functions. The vertex is written as

$$\tilde{\mathcal{L}}_{VBB} = g q \bar{q} \gamma^\mu \epsilon_\mu, \quad (3)$$

where  $q \bar{q}$  is the quark wave function of the exchanged vector meson, and at low energies we take  $\gamma^\mu \sim \gamma^0 \sim 1$ . Then we obtain the corresponding potential

$$V_{ij} = \frac{1}{4f^2} C_{ij} (k^0 + k'^0) \vec{\epsilon} \vec{\epsilon}', \quad (4)$$

where  $k^0$ ,  $k'^0$  ( $\vec{\epsilon}$ ,  $\vec{\epsilon}'$ ) are the energies in the meson-baryon rest frame (spin polarization vectors) of the initial and final mesons, respectively. The coefficient matrix  $C_{ij}$  with the channels  $\bar{K}^* \Xi^*$  ( $I = 0$ ) (1),  $\omega \Omega$  (2) and  $\phi \Omega$  (3), is given by

$$C_{ij} = \begin{pmatrix} 0 & \sqrt{3} & -\sqrt{6} \\ & 0 & 0 \\ & & 0 \end{pmatrix}, \quad (5)$$

which is the same as Table 8 of Ref. [48], but a global sign difference because of the phase factor introduced by coupling here  $VB$ , instead of  $BV$  taken in Ref. [48]. The isospin  $I = 0$   $\bar{K}^* \Xi^*$  is given with the isospin phase convention  $(\bar{K}^{*0}, -K^{*-})$  and  $(\Xi^{*0}, \Xi^{*-})$  as

$$|\bar{K}^* \Xi^*, I = 0\rangle = \frac{1}{\sqrt{2}} (\bar{K}^{*0} \Xi^{*-} + K^{*-} \Xi^{*0}). \quad (6)$$

The scattering amplitude is then obtained by solving the Bethe–Salpeter equation

$$T = [1 - VG]^{-1} V, \quad (7)$$

where  $G$  is the loop function

$$G_i(\sqrt{s}) = 2M_i \int_{|\vec{q}| < q_{\max}} \frac{d^3 q}{(2\pi)^3} \frac{\omega_i(\vec{q}) + E_i(\vec{q})}{2\omega_i(\vec{q}) E_i(\vec{q})} \frac{1}{s - (\omega_i(\vec{q}) + E_i(\vec{q}))^2 + i\epsilon}, \quad (8)$$

with  $M_i$  the baryon mass and  $\omega_i(\vec{q})$ ,  $E_i(\vec{q})$  the meson, baryon energy, respectively. For the  $\bar{K}^* \Xi^*$  channel, we also consider the mass distributions of  $\bar{K}^*$  and  $\Xi^*$ , and perform a double convolution

$$\tilde{G}_{\bar{K}^* \Xi^*}(\sqrt{s}) = \frac{1}{N} \int_{(m_{\bar{K}^*} - 2\Gamma_{\bar{K}^*})^2}^{(m_{\bar{K}^*} + 2\Gamma_{\bar{K}^*})^2} d\tilde{m}^2 \left( -\frac{1}{\pi} \right) \text{Im} \left( \frac{1}{\tilde{m}^2 - m_{\bar{K}^*}^2 + im_{\bar{K}^*} \Gamma_{\bar{K}^*}} \right)$$

$$\times \int_{M_{\Xi^*} - 2\Gamma_{\Xi^*}}^{M_{\Xi^*} + 2\Gamma_{\Xi^*}} d\tilde{M} \left( -\frac{1}{\pi} \right) \text{Im} \left( \frac{1}{\tilde{M} - M_{\Xi^*} + i\frac{\Gamma_{\Xi^*}}{2}} \right) G_{\bar{K}^* \Xi^*}(\tilde{m}, \tilde{M}, \sqrt{s}), \quad (9)$$

with

$$N = \int_{(M_{\bar{K}^*} - 2\Gamma_{\bar{K}^*})^2}^{(M_{\bar{K}^*} + 2\Gamma_{\bar{K}^*})^2} d\tilde{m}^2 \left( -\frac{1}{\pi} \right) \text{Im} \left( \frac{1}{\tilde{m}^2 - m_{\bar{K}^*}^2 + im_{\bar{K}^*}\Gamma_{\bar{K}^*}} \right) \\ \times \int_{M_{\Xi^*} - 2\Gamma_{\Xi^*}}^{M_{\Xi^*} + 2\Gamma_{\Xi^*}} d\tilde{M} \left( -\frac{1}{\pi} \right) \text{Im} \left( \frac{1}{\tilde{M} - M_{\Xi^*} + i\frac{\Gamma_{\Xi^*}}{2}} \right). \quad (10)$$

Thus, the  $G$  matrix entering in Eq. (7) can be expressed as

$$G = \begin{pmatrix} \tilde{G}_{\bar{K}^* \Xi^*} \\ & G_{\omega\Omega} \\ & & G_{\phi\Omega} \end{pmatrix}. \quad (11)$$

### A. Box Diagrams

The inclusion of the  $\bar{K}^*$  and  $\Xi^*$  widths in Eq. (9) already provides a finite width to the possible bound states generated in the coupled-channel approach. However, in order to establish a connection with the experimentally observed  $\Omega(2380)$ , it is necessary to account explicitly for its dominant decay modes. According to the PDG [47], these are  $\Xi^- \pi^+ K^-$ ,  $\Xi(1530)^0 K^-$ , and  $\Xi^- \bar{K}^{*0}$ . Within the present framework, the two-body decay channels arise naturally through the transitions  $\bar{K}^* \Xi^* \rightarrow \bar{K} \Xi^*$  and  $\bar{K}^* \Xi^* \rightarrow \bar{K}^* \Xi$ . Their contribution is incorporated by evaluating the corresponding box diagrams, with  $\bar{K} \Xi^*$  and  $\bar{K}^* \Xi$  as intermediate states. The use of box diagrams to account for the width of dynamically generated states is well established in the literature [57–62]. In this work, only the imaginary part of the box diagrams is retained, since the real part has been shown to be small and can be neglected [57, 58]. The box diagrams corresponding to the  $\bar{K}^* \Xi^*$  decays into  $\bar{K} \Xi^*$  and  $\bar{K}^* \Xi$  are shown in Figs. 2 and 3, respectively.

#### 1. Box diagrams with $\bar{K} \Xi^*$ intermediate states

In total, six box diagrams contribute to this process. However, it is sufficient to evaluate a single diagram explicitly, since the remaining ones can be obtained by applying isospin symmetry through the appropriate Clebsch–Gordan coefficients.

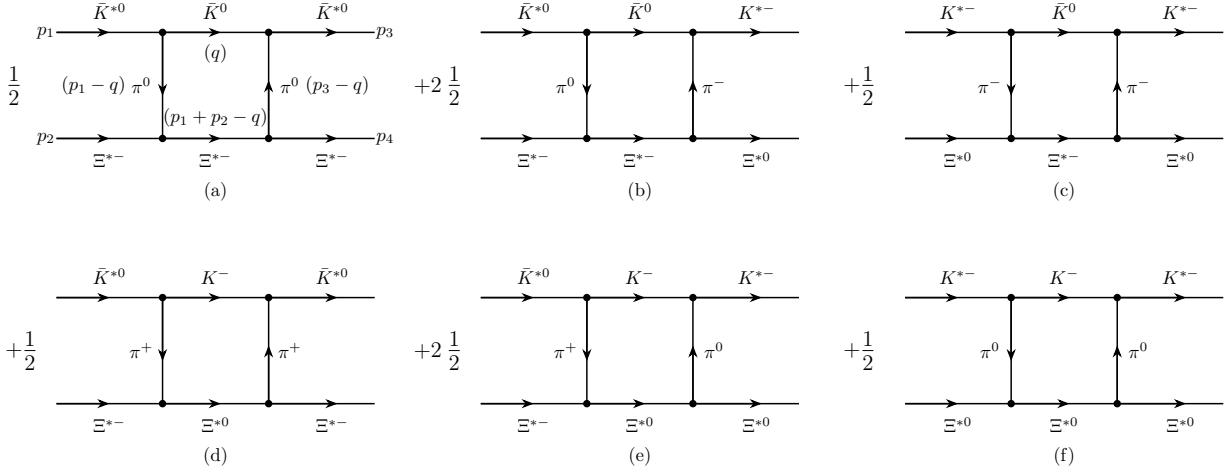


FIG. 2. Box diagrams for  $\bar{K}^* \Xi^*$  decay into  $\bar{K} \Xi^*$ .

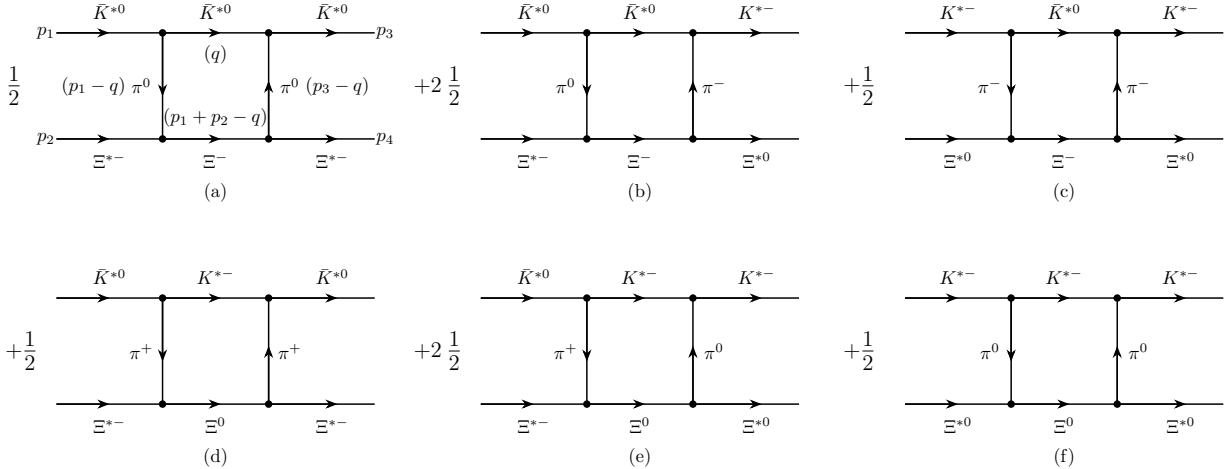


FIG. 3. Box diagrams for  $\bar{K}^* \Xi^*$  decay into  $\bar{K}^* \Xi$ .

Furthermore, since we are working close to threshold, the three-momenta of the external particles can be neglected in comparison with the vector-meson mass. We therefore set

$$\vec{p}_1 = \vec{p}_2 = \vec{p}_3 = \vec{p}_4 = 0. \quad (12)$$

The evaluation of the box diagrams in Fig. 2 requires two types of vertices: the ordinary  $VPP$  coupling and the  $\pi \Xi^* \Xi^*$  coupling. We first focus on the diagram of Fig. 2(a), which contains four vertices  $\bar{K}^{*0} \rightarrow \pi^0 \bar{K}^0$ ,  $\pi^0 \bar{K}^0 \rightarrow \bar{K}^{*0}$ ,  $\Xi^{*-} \rightarrow \pi^0 \Xi^{*-}$ ,  $\pi^0 \Xi^{*-} \rightarrow \Xi^{*-}$ . The upper two  $VPP$  vertices are obtained from the Lagrangian

$$\mathcal{L}_{VPP} = -ig \langle [P, \partial_\mu P] \cdot V^\mu \rangle, \quad (13)$$

with the matrix of the pseudoscalar mesons given by

$$P = \begin{pmatrix} \frac{\pi^0}{\sqrt{2}} + \frac{\eta}{\sqrt{3}} & \pi^+ & K^+ \\ \pi^- & -\frac{\pi^0}{\sqrt{2}} + \frac{\eta}{\sqrt{3}} & K^0 \\ K^- & \bar{K}^0 & -\frac{\eta}{\sqrt{3}} \end{pmatrix}, \quad (14)$$

where the standard  $\eta$ - $\eta'$  mixing is taken into account, following Ref. [63], and the  $\eta'$  contribution is subsequently neglected, since it is too massive to play a role in the present analysis. Hence the  $\bar{K}^{*0} \rightarrow \pi^0 \bar{K}^0$  vertex goes as

$$-it = i\mathcal{L}_{VPP} = i\sqrt{2} g \vec{\epsilon}_{\bar{K}^{*0}} \vec{q}, \quad (15)$$

where we take  $\epsilon_{\bar{K}^{*0}}^0 = 0$  since the  $\bar{K}^*$  three momentum is neglected. The  $\pi^0 \bar{K}^0 \rightarrow \bar{K}^{*0}$  vertex is described by the same amplitude.

Next, we require the  $\pi \Xi^* \Xi^*$  vertex. To this end, we begin by considering the coupling of  $\pi$  with two  $\frac{1}{2}^+$  baryons, assuming the  $\pi$  momentum  $\vec{q}$  in the  $z$  direction and entering the baryon line, which is given by [64]

$$-it_{\pi BB'} = \vec{\sigma} \vec{q} \langle B' | \tilde{V}_\pi | B \rangle, \quad (16)$$

where  $B, B'$  denote the quark wave functions of baryons. The operator  $\tilde{V}_\pi$  reads

$$\tilde{V}_\pi = \frac{3}{5} \frac{f_{\pi NN}}{m_\pi} \sqrt{2} \sum_i \left\{ \frac{1}{\sqrt{2}} (u\bar{u} - d\bar{d}) \right\}_i \sigma_{z,i}, \quad (17)$$

where the index  $i$  runs over the quarks in the baryon,  $f_{\pi NN}$  is the  $\pi^0 pp$  coupling constant (set to  $f_{\pi NN} = 1$  in the present work), and  $m_\pi$  is the pion mass. In Eq. (17),  $\sigma_z$  is the ordinary quark spin matrix for spin  $\frac{1}{2}$  in  $z$  direction. The three components in the bracket of Eq. (17) stand for  $\pi^+, \pi^0, \pi^-$  fields, respectively. This operator for the case of the  $\pi^0 pp$  vertex, leads to the macroscopic vertex

$$-it = \frac{f_{\pi NN}}{m_\pi} \vec{\sigma} \vec{q}, \quad (18)$$

where  $\vec{\sigma}$  denotes the spin operator of the proton.

We now turn to the  $\pi\Xi^*\Xi^*$  coupling. At the macroscopic level for  $J^P = \frac{3}{2}^+$  baryons, the spin operator is  $\tilde{S} \cdot \vec{q}$ . In the spherical basis, this operator can be written as

$$\tilde{S} \cdot \vec{q} = \sum_{\mu} (-1)^{\mu} \tilde{S}_{\mu} q_{-\mu}, \quad (19)$$

$$\text{with } \begin{cases} q_{+1} = -\frac{1}{\sqrt{2}}(q_x + iq_y) \\ q_{-1} = \frac{1}{\sqrt{2}}(q_x - iq_y) \\ q_0 = q_z \end{cases} \text{ and } \begin{cases} \tilde{S}_{+1} = -\frac{1}{\sqrt{2}}(S_x + iS_y) \\ \tilde{S}_{-1} = \frac{1}{\sqrt{2}}(S_x - iS_y) \\ \tilde{S}_0 = S_z \end{cases}.$$

To evaluate the  $\Xi^{*-} \rightarrow \pi^0 \Xi^{*-}$  vertex shown in Fig 2(a), Eq. (17) is used together with the spin-flavor quark wave function

$$\Phi_{\Xi^{*-}} = \frac{1}{\sqrt{3}} |dss + sds + ssd\rangle \chi_s, \quad (20)$$

with  $\chi_s$  the spin symmetric wave function.

The matrix elements of the spin transition operator  $\tilde{S}_{\mu}$  are expressed in terms of Clebsch-Gordan coefficients using the Wigner-Eckart theorem,

$$\langle M' | \tilde{S}_{\mu} | M \rangle = \alpha \mathcal{C}(\frac{3}{2} \ 1 \ \frac{3}{2}; M \ \mu \ M'), \quad (21)$$

which properly evaluated with  $\mu = 0$  and  $M = M' = \frac{3}{2}$  renders

$$\alpha = \frac{1}{2} \sqrt{15}. \quad (22)$$

Next, taking into account Eqs. (17), (20) and the  $\chi_s$  wave function of [65], one finds

$$\langle \Xi^{*-}, \tilde{S}_z = \frac{3}{2} | \tilde{V}_{\pi} | \Xi^{*-}, \tilde{S}_z = \frac{3}{2} \rangle = -\frac{3}{5} \frac{f_{\pi NN}}{m_{\pi}}. \quad (23)$$

This result can be matched to a macroscopic operator of the form  $\langle M' | \beta \tilde{S} \cdot \vec{q} | M \rangle$ , which fixes  $\beta = -\frac{2}{5} \frac{f_{\pi NN}}{m_{\pi}}$ . Accordingly, we obtain

$$-it = -\frac{2}{5} \frac{f_{\pi NN}}{m_{\pi}} \tilde{S} \cdot \vec{q}. \quad (24)$$

The  $\Xi^{*-} \pi^0 \rightarrow \Xi^{*-}$  vertex has the same coupling strength, with an additional minus sign arising from the reversed momentum flow of the  $\pi^0$ . Combining both vertices, the contribution of the two lower vertices is given by

$$-\frac{4}{25} \left( \frac{f_{\pi NN}}{m_{\pi}} \right)^2 \sum_M \langle S_4 | \tilde{S} \cdot \vec{q} | M \rangle \langle M | \tilde{S} \cdot \vec{q} | S_2 \rangle, \quad (25)$$

where  $S_2$ ,  $S_4$  and  $M$  are the third component of the spin of the initial, final and intermediate  $\Xi^{*-}$ , respectively.

The diagrams of Fig. 2 are evaluated by averaging over spins for diagonal transitions,  $S_2 = S_4$ . In general, one has

$$\begin{aligned} \left\langle S_4 \left| \tilde{S} \cdot \vec{q} \right| M \right\rangle \left\langle M \left| \tilde{S} \cdot \vec{q} \right| S_4 \right\rangle &= \left\langle S_4 \left| \sum_{\mu} (-1)^{\mu} S_{\mu} q_{-\mu} \right| M \right\rangle \left\langle M \left| \sum_{\nu} (-1)^{\nu} S_{-\nu} q_{\nu} \right| S_4 \right\rangle \\ &= \sum_{\mu} (-1)^{\mu} \alpha \mathcal{C}(\frac{3}{2} 1 \frac{3}{2}; M \mu S_4) q_{-\mu} \sum_{\nu} (-1)^{\nu} \alpha \mathcal{C}(\frac{3}{2} 1 \frac{3}{2}; S_4 - \nu M) q_{\nu}, \end{aligned} \quad (26)$$

where conditions  $M + \mu = S_4$  and  $S_4 - \nu = M$  enforce  $\mu = \nu$ . Permuting the indices  $S_4$ ,  $M$  in the second Clebsch-Gordan coefficient [66], one obtains

$$\sum_{\mu} (-1)^{\mu} \alpha^2 q_{-\mu} q_{\mu} \mathcal{C}(\frac{3}{2} 1 \frac{3}{2}; M \mu S_4) \mathcal{C}(\frac{3}{2} 1 \frac{3}{2}; M \mu S_4). \quad (27)$$

Summing Eq. (27) over the intermediate spin projection  $M$ , the orthogonality of the Clebsch-Gordan coefficients yields  $\delta_{\frac{3}{2} \frac{3}{2}}$  and one finally finds

$$\frac{1}{4} \sum_{S_4} \sum_M \left\langle S_4 \left| \tilde{S} \cdot \vec{q} \right| M \right\rangle \left\langle M \left| \tilde{S} \cdot \vec{q} \right| S_4 \right\rangle = \frac{1}{4} \alpha^2 \sum_{\mu} (-1)^{\mu} q_{-\mu} q_{\mu} = \frac{1}{4} \alpha^2 \vec{q}^2 = \frac{15}{16} \vec{q}^2. \quad (28)$$

Substituting this result into Eq. (25), we obtain

$$\begin{aligned} (1) \Xi^{*-} &\xrightarrow{\pi} \Xi^{*-} \xrightarrow{\pi} \Xi^{*-} : -\frac{4}{25} \left( \frac{f_{\pi NN}}{m_{\pi}} \right)^2 \frac{15}{16} \vec{q}^2; \\ (2) \Xi^{*-} &\xrightarrow{\pi} \Xi^{*-} \xrightarrow{\pi} \Xi^{*0} : \frac{4\sqrt{2}}{25} \left( \frac{f_{\pi NN}}{m_{\pi}} \right)^2 \frac{15}{16} \vec{q}^2; \\ (3) \Xi^{*0} &\xrightarrow{\pi} \Xi^{*-} \xrightarrow{\pi} \Xi^{*0} : -\frac{8}{25} \left( \frac{f_{\pi NN}}{m_{\pi}} \right)^2 \frac{15}{16} \vec{q}^2; \\ (4) \Xi^{*-} &\xrightarrow{\pi} \Xi^{*0} \xrightarrow{\pi} \Xi^{*-} : -\frac{8}{25} \left( \frac{f_{\pi NN}}{m_{\pi}} \right)^2 \frac{15}{16} \vec{q}^2; \\ (5) \Xi^{*-} &\xrightarrow{\pi} \Xi^{*0} \xrightarrow{\pi} \Xi^{*0} : -\frac{4\sqrt{2}}{25} \left( \frac{f_{\pi NN}}{m_{\pi}} \right)^2 \frac{15}{16} \vec{q}^2; \\ (6) \Xi^{*0} &\xrightarrow{\pi} \Xi^{*0} \xrightarrow{\pi} \Xi^{*0} : -\frac{4}{25} \left( \frac{f_{\pi NN}}{m_{\pi}} \right)^2 \frac{15}{16} \vec{q}^2. \end{aligned} \quad (29)$$

We next turn to the upper vertices of the diagrams, which are of the type given in Eq. (15). The resulting structure of box diagrams is of the form

$$\int d^3 q \vec{\epsilon} \vec{q} \vec{\epsilon}' \vec{q} f(q^2) = \int d^3 q \epsilon_i \epsilon'_j q_i q_j f(q^2) = \frac{1}{3} \epsilon_i \epsilon'_j \delta_{ij} \int d^3 q \vec{q}^2 f(q^2), \quad (30)$$

which allows one to write the contribution of the two upper vertices as

$$\begin{aligned}
(1) \bar{K}^{*0} &\xrightarrow{\pi} \bar{K}^0 \xrightarrow{\pi} \bar{K}^{*0} : -\frac{2}{3}g^2\vec{q}^2\vec{\epsilon}\vec{\epsilon}'; \\
(2) \bar{K}^{*0} &\xrightarrow{\pi} \bar{K}^0 \xrightarrow{\pi} K^{*-} : \frac{2\sqrt{2}}{3}g^2\vec{q}^2\vec{\epsilon}\vec{\epsilon}'; \\
(3) K^{*-} &\xrightarrow{\pi} \bar{K}^0 \xrightarrow{\pi} K^{*-} : -\frac{4}{3}g^2\vec{q}^2\vec{\epsilon}\vec{\epsilon}'; \\
(4) \bar{K}^{*0} &\xrightarrow{\pi} K^- \xrightarrow{\pi} \bar{K}^{*0} : -\frac{4}{3}g^2\vec{q}^2\vec{\epsilon}\vec{\epsilon}'; \\
(5) \bar{K}^{*0} &\xrightarrow{\pi} K^- \xrightarrow{\pi} K^{*-} : -\frac{2\sqrt{2}}{3}g^2\vec{q}^2\vec{\epsilon}\vec{\epsilon}'; \\
(6) K^{*-} &\xrightarrow{\pi} K^- \xrightarrow{\pi} K^{*-} : -\frac{2}{3}g^2\vec{q}^2\vec{\epsilon}\vec{\epsilon}'.
\end{aligned} \tag{31}$$

Having evaluated all the vertices, we now compute the total amplitude of the box diagram in Fig. 2. Starting with Fig. 2(a), and setting  $\vec{p}_1 = \vec{p}_2 = \vec{p}_3 = \vec{p}_4 = 0$ , the corresponding amplitude reads

$$\begin{aligned}
\tilde{V}_{\bar{K}\Xi^*(a)} = &i \int \frac{d^4q}{(2\pi)^4} \left( -\frac{2}{3}g^2\vec{q}^2 \right) \left[ -\frac{4}{25} \left( \frac{f_{\pi NN}}{m_\pi} \right)^2 \frac{15}{16} \vec{q}^2 \right] \frac{i}{(p_1 - q)^2 - m_\pi^2 + i\epsilon} \frac{i}{(p_3 - q)^2 - m_\pi^2 + i\epsilon} \\
&\times \frac{1}{2\omega_{\bar{K}}(\vec{q})} \frac{i}{q^0 - \omega_{\bar{K}}(\vec{q}) + i\epsilon} \frac{M_{\Xi^*}}{E_{\Xi^*}(\vec{q})} \frac{i}{p_1^0 + p_2^0 - q^0 - E_{\Xi^*}(\vec{q}) + i\epsilon} \vec{\epsilon}\vec{\epsilon}', \tag{32}
\end{aligned}$$

with

$$p_1^0 = p_3^0 = \frac{M_{inv}^2 + m_{\bar{K}^*}^2 - M_{\Xi^*}^2}{2M_{inv}}, \tag{33}$$

$$p_2^0 = p_4^0 = \frac{M_{inv}^2 + M_{\Xi^*}^2 - m_{\bar{K}^*}^2}{2M_{inv}}. \tag{34}$$

As discussed above, we are only interested in the imaginary part of the diagram that arises when the intermediate  $\bar{K}\Xi^*$  states are placed on shell. For this purpose, it is convenient to separate the positive- and negative-energy parts of the propagator as

$$\frac{1}{q^2 - m^2 + i\epsilon} = \frac{1}{2\omega(\vec{q})} \left( \frac{1}{q^0 - \omega(\vec{q}) + i\epsilon} - \frac{1}{q^0 + \omega(\vec{q}) - i\epsilon} \right) \tag{35}$$

and retain only the first term. This prescription has already been implemented in Eq. (32). For the baryon propagator we have the same, but keeping the field normalization of Mandl and Shaw [67]. For the exchanged pions, which are necessarily off shell, we keep the full propagators. Then, we can perform an analytical integration over the variable  $q^0$ , using Cauchy's residue theorem (alternatively, one may use Cutkosky rules). As a result, Eq. (32) takes the form

$$\tilde{V}_{\bar{K}\Xi^*(a)} = \int \frac{d^3q}{(2\pi)^3} \left( -\frac{2}{3}g^2\vec{q}^2 \right) \left[ -\frac{4}{25} \left( \frac{f_{\pi NN}}{m_\pi} \right)^2 \frac{15}{16} \vec{q}^2 \right] \left( \frac{1}{(p_1^0 - \omega_{\bar{K}}(\vec{q}))^2 - \omega_\pi(\vec{q})^2 + i\epsilon} \right)^2$$

$$\times \frac{1}{2\omega_{\bar{K}}(\vec{q})} \frac{M_{\Xi^*}}{E_{\Xi^*}(\vec{q})} \frac{1}{p_1^0 + p_2^0 - \omega_{\bar{K}}(\vec{q}) - E_{\Xi^*}(\vec{q}) + i\epsilon} \vec{\epsilon} \vec{\epsilon}''. \quad (36)$$

Using  $i \operatorname{Im}(\frac{1}{x+i\epsilon}) = -i\pi\delta(x)$  we then obtain

$$\begin{aligned} \operatorname{Im}\tilde{V}_{\bar{K}\Xi^*(a)} &= -\frac{M_{\Xi^*}}{4\pi} \frac{\vec{q}}{M_{inv}} \left( -\frac{2}{3} g^2 \vec{q}^2 \right) \left[ -\frac{4}{25} \left( \frac{f_{\pi NN}}{m_\pi} \right)^2 \frac{15}{16} \vec{q}^2 \right] \left( \frac{1}{(p_1^0 - \omega_{\bar{K}}(\vec{q}))^2 - \omega_\pi(\vec{q})^2 + i\epsilon} \right)^2 \vec{\epsilon} \vec{\epsilon}' \\ &= -\frac{1}{10} \vec{\epsilon} \vec{\epsilon}' g^2 \vec{q}^5 \frac{M_{\Xi^*}}{4\pi} \left( \frac{f_{\pi NN}}{m_\pi} \right)^2 \frac{1}{M_{inv}} \left( \frac{1}{(p_1^0 - \omega_{\bar{K}}(\vec{q}))^2 - \omega_\pi(\vec{q})^2 + i\epsilon} \right)^2, \end{aligned} \quad (37)$$

with

$$|\vec{q}| = \frac{\lambda^{\frac{1}{2}} (M_{inv}^2, m_{\bar{K}}^2, M_{\Xi^*}^2)}{2M_{inv}}. \quad (38)$$

Summing the six diagrams shown in Fig. 2, with the corresponding weights of Eqs. (29) and (31), the total imaginary part of the amplitude is written as

$$\operatorname{Im}\tilde{V}_{\bar{K}\Xi^*} = -\frac{9}{10} \vec{\epsilon} \vec{\epsilon}' g^2 \vec{q}^5 \frac{M_{\Xi^*}}{4\pi} \left( \frac{f_{\pi NN}}{m_\pi} \right)^2 \frac{1}{M_{inv}} \left( \frac{1}{(p_1^0 - \omega_{\bar{K}}(\vec{q}))^2 - \omega_\pi(\vec{q})^2 + i\epsilon} \right)^2 FF(\vec{q})^2, \quad (39)$$

where, since the pions are off shell, we introduce a form factor  $FF(\vec{q})$ , defined as [61]

$$FF(\vec{q}) = e^{[(p_1^0 - q^0)^2 - \vec{q}^2]/\Lambda^2}, \quad (40)$$

with

$$q^0 = \frac{M_{inv}^2 + m_{\bar{K}}^2 - M_{\Xi^*}^2}{2M_{inv}}. \quad (41)$$

In the numerical evaluation we take  $\Lambda \simeq 1$  GeV.

## 2. Box diagrams with $\bar{K}^*\Xi$ intermediate states

To evaluate the box diagrams in Fig. 3, two additional types of vertices are required: the anomalous  $VVP$  coupling and the  $\pi\Xi\Xi^*$  coupling. The upper  $VVP$  vertex is given by the Lagrangian [63]

$$\mathcal{L}_{VVP} = \frac{G'}{\sqrt{2}} \epsilon^{\mu\nu\alpha\beta} \langle \partial_\mu V_\nu \partial_\alpha V_\beta P \rangle, \quad (42)$$

with coupling constants  $G' = \frac{3g'^2}{4\pi^2 f_\pi}$ ,  $g' = -\frac{G_v m_\rho}{\sqrt{2} f_\pi^2}$ ,  $G_v = 55$  MeV ( $G' \approx 14$  GeV $^{-1}$ ).

We start with Fig. 3(a), the  $\bar{K}^{*0} \rightarrow \pi^0 \bar{K}^{*0}$  vertex goes as ( $\epsilon^{\mu\nu\alpha\beta} = \epsilon^{\alpha\beta\mu\nu}$ )

$$-it = i\mathcal{L}_{\text{VVP}} = -i \frac{G'}{\sqrt{2}} \frac{1}{\sqrt{2}} \epsilon^{\alpha\beta\mu\nu} (-ip_{1\alpha}) \epsilon_{\beta(in)} (iq_\mu) \epsilon_{\nu(out)}, \quad (43)$$

where *in* and *out* represent the incoming (in this case the initial) and outgoing (in this case the intermediate)  $\bar{K}^{*0}$ . One should notice that since  $\vec{p}_1 = 0$ , we need to take  $\alpha = 0$ , then  $\epsilon^{\alpha\beta\mu\nu} = \epsilon^{0\beta\mu\nu} = \epsilon^{ijk}$ , and an extra minus sign comes from raising the covariant indices. So that Eq. (43) becomes

$$-it = i \frac{G'}{\sqrt{2}} \frac{1}{\sqrt{2}} \epsilon^{ijk} p_1^0 \epsilon_{(in)}^i q^j \epsilon_{(out)}^k. \quad (44)$$

Similarly, the  $\bar{K}^{*0} \pi^0 \rightarrow \bar{K}^{*0}$  vertex is written with the same structure

$$-it = -i \frac{G'}{\sqrt{2}} \frac{1}{\sqrt{2}} \epsilon^{ijk} p_3^0 \epsilon_{(in)}^i q^j \epsilon_{(out)}^k. \quad (45)$$

But in this case *in* and *out* correspond to the intermediate and final  $\bar{K}^{*0}$ , respectively. When combining these two vertices via the intermediate  $\bar{K}^{*0}$ , we must contract the polarization vectors of this intermediate meson, that is  $\epsilon_{(out)}^k$  in Eq. (44) and  $\epsilon_{(in)}^i$  in Eq. (45).

For the  $\pi \Xi \Xi^*$  coupling, we introduce two spin transition operators at the hadron level:  $\vec{S} \cdot \vec{q}$  for the transition from spin  $\frac{3}{2}$  to  $\frac{1}{2}$ , and  $\vec{S}^+ \cdot \vec{q}$  for the inverse process. According to the Wigner–Eckart theorem, we have [64]

$$\left\langle \frac{3}{2} M \left| S_\mu^+ \right| \frac{1}{2} m \right\rangle = \mathcal{C} \left( \frac{1}{2} 1 \frac{3}{2}; m \mu M \right) \left\langle \frac{3}{2} \left\| \vec{S}^+ \right\| \frac{1}{2} \right\rangle, \quad (46)$$

where  $\mu$  denotes the spherical component of  $\vec{S}^+$ . The reduced matrix element is set to unity:  $\left\langle \frac{3}{2} \left\| \vec{S}^+ \right\| \frac{1}{2} \right\rangle \equiv 1$ .

In Fig. 3(a), we evaluate the  $\Xi^{*-} \rightarrow \pi^0 \Xi^-$  and  $\pi^0 \Xi^- \rightarrow \Xi^{*-}$  vertices. Using Eq. (17) with the quark wave function of the baryon, and mapping the quark-level operators to hadron spin operators as before, the vertex amplitudes are

$$-it_{\Xi^{*-} \rightarrow \pi^0 \Xi^-} = -\frac{2}{5} \sqrt{3} \frac{f_{\pi NN}}{m_\pi} \vec{S} \cdot (-\vec{q}), \quad (47)$$

$$-it_{\pi^0 \Xi^- \rightarrow \Xi^{*-}} = -\frac{2}{5} \sqrt{3} \frac{f_{\pi NN}}{m_\pi} \vec{S}^+ \cdot \vec{q}. \quad (48)$$

As in Sec. II A 1, we consider only diagonal transitions for  $\Xi^*$  ( $M = M'$ ) and average over the spin projections ( $M$ ). Thus, we have

$$\frac{1}{4} \sum_M \sum_m \left\langle M \left| \vec{S}^+ \vec{q} \right| m \right\rangle \left\langle m \left| \vec{S} \vec{q} \right| M \right\rangle = \frac{1}{4} \sum_m \sum_M \left\langle m \left| \vec{S} \vec{q} \right| M \right\rangle \left\langle M \left| \vec{S}^+ \vec{q} \right| m \right\rangle \quad (49)$$

and using the spin-sum identity,

$$\sum_M \langle m' | S_i | M \rangle \langle M | S_j^+ | m \rangle = \left\langle m' \left| \frac{2}{3} \delta_{ij} - \frac{i}{3} \epsilon_{ijk} \sigma_k \right| m \right\rangle, \quad (50)$$

the spin sum for the two lower vertices gives an overall factor of  $\frac{1}{4} 2 \frac{2}{3} \vec{q}^2$ . This leads to the contributions from the six possible lower-vertex transitions:

$$\begin{aligned} (1) \Xi^{*-} &\xrightarrow{\pi} \Xi^- \xrightarrow{\pi} \Xi^{*-} : -\frac{4}{25} \left( \frac{f_{\pi NN}}{m_\pi} \right)^2 \vec{q}^2; \\ (2) \Xi^{*-} &\xrightarrow{\pi} \Xi^- \xrightarrow{\pi} \Xi^{*0} : \frac{4\sqrt{2}}{25} \left( \frac{f_{\pi NN}}{m_\pi} \right)^2 \vec{q}^2; \\ (3) \Xi^{*0} &\xrightarrow{\pi} \Xi^- \xrightarrow{\pi} \Xi^{*0} : -\frac{8}{25} \left( \frac{f_{\pi NN}}{m_\pi} \right)^2 \vec{q}^2; \\ (4) \Xi^{*-} &\xrightarrow{\pi} \Xi^0 \xrightarrow{\pi} \Xi^{*-} : -\frac{8}{25} \left( \frac{f_{\pi NN}}{m_\pi} \right)^2 \vec{q}^2; \\ (5) \Xi^{*-} &\xrightarrow{\pi} \Xi^0 \xrightarrow{\pi} \Xi^{*0} : -\frac{4\sqrt{2}}{25} \left( \frac{f_{\pi NN}}{m_\pi} \right)^2 \vec{q}^2; \\ (6) \Xi^{*0} &\xrightarrow{\pi} \Xi^0 \xrightarrow{\pi} \Xi^{*0} : -\frac{4}{25} \left( \frac{f_{\pi NN}}{m_\pi} \right)^2 \vec{q}^2. \end{aligned} \quad (51)$$

Using these results, we now consider the upper VVP vertices in Eqs. (44) and (45). Summing over the polarization of the intermediate  $\bar{K}^*$ , the relevant contraction reads

$$\begin{aligned} \sum_{\tilde{\epsilon}_{\text{pole}}} \epsilon^{ijk} \epsilon^{i'j'k'} \epsilon_i q_j \tilde{\epsilon}_k \epsilon'_{i'} q_{j'} \tilde{\epsilon}_{k'} &= \epsilon^{ijk} \epsilon^{i'j'k'} \epsilon_i q_j \epsilon'_{i'} q_{j'} \delta_{kk'} \\ &= \epsilon^{ijk} \epsilon^{i'j'k} \epsilon_i q_j \epsilon'_{i'} q_{j'} \\ &\rightarrow \epsilon^{ijk} \epsilon^{i'j'k} \epsilon_i \epsilon'_{i'} \frac{1}{3} \vec{q}^2 \delta_{jj'} \\ &= \frac{2}{3} \vec{q}^2 \vec{\epsilon} \vec{\epsilon}', \end{aligned} \quad (52)$$

where, in the last step, we used the standard angular average  $\int d^3q q_i q_j f(q^2) = \frac{1}{3} \delta_{ij} \int d^3q \vec{q}^2 f(q^2)$ , which is valid since the lower vertices now depend only on  $\vec{q}^2$ . With this, the contribution

from the upper vertices is given by

$$\begin{aligned}
(1) \bar{K}^{*0} &\xrightarrow{\pi} \bar{K}^{*0} \xrightarrow{\pi} \bar{K}^{*0} : -\frac{1}{3} \left( \frac{G'}{\sqrt{2}} \right)^2 (p_1^0)^2 \vec{q}^2 \vec{\epsilon} \vec{\epsilon}' ; \\
(2) \bar{K}^{*0} &\xrightarrow{\pi} \bar{K}^{*0} \xrightarrow{\pi} K^{*-} : \sqrt{2} \frac{1}{3} \left( \frac{G'}{\sqrt{2}} \right)^2 (p_1^0)^2 \vec{q}^2 \vec{\epsilon} \vec{\epsilon}' ; \\
(3) K^{*-} &\xrightarrow{\pi} \bar{K}^{*0} \xrightarrow{\pi} K^{*-} : -2 \frac{1}{3} \left( \frac{G'}{\sqrt{2}} \right)^2 (p_1^0)^2 \vec{q}^2 \vec{\epsilon} \vec{\epsilon}' ; \\
(4) \bar{K}^{*0} &\xrightarrow{\pi} K^{*-} \xrightarrow{\pi} \bar{K}^{*0} : -2 \frac{1}{3} \left( \frac{G'}{\sqrt{2}} \right)^2 (p_1^0)^2 \vec{q}^2 \vec{\epsilon} \vec{\epsilon}' ; \\
(5) \bar{K}^{*0} &\xrightarrow{\pi} K^{*-} \xrightarrow{\pi} K^{*-} : -\sqrt{2} \frac{1}{3} \left( \frac{G'}{\sqrt{2}} \right)^2 (p_1^0)^2 \vec{q}^2 \vec{\epsilon} \vec{\epsilon}' ; \\
(6) K^{*-} &\xrightarrow{\pi} K^{*-} \xrightarrow{\pi} K^{*-} : -\frac{1}{3} \left( \frac{G'}{\sqrt{2}} \right)^2 (p_1^0)^2 \vec{q}^2 \vec{\epsilon} \vec{\epsilon}' ,
\end{aligned} \tag{53}$$

with  $\vec{\epsilon}$  and  $\vec{\epsilon}'$  the spin polarization vectors of the initial and final  $\bar{K}^*$ , respectively.

Finally, summing all contributions from the six diagrams in Fig. 3, the imaginary part of the full  $\bar{K}^* \Xi$  box amplitude is

$$\text{Im} \tilde{V}_{\bar{K}^* \Xi} = -\frac{6}{25} \vec{\epsilon} \vec{\epsilon}' G'^2 (p_1^0)^2 \vec{q}^5 \frac{M_\Xi}{4\pi} \left( \frac{f_{\pi NN}}{m_\pi} \right)^2 \frac{1}{M_{inv}} \left( \frac{1}{(p_1^0 - \omega_{\bar{K}^*}(\vec{q}))^2 - \omega_\pi(\vec{q})^2 + i\epsilon} \right)^2 F F(\vec{q})^2 , \tag{54}$$

where the intermediate three-momentum and energy in the center-of-mass frame are

$$|\vec{q}| = \frac{\lambda^{\frac{1}{2}} (M_{inv}^2, m_{\bar{K}^*}^2, M_\Xi^2)}{2M_{inv}} , \tag{55}$$

$$q^0 = \frac{M_{inv}^2 + m_{\bar{K}^*}^2 - M_\Xi^2}{2M_{inv}} . \tag{56}$$

These expressions are analogous to those of the  $\bar{K} \Xi^*$  case (see Eqs. (38) and (41)), but differ due to the different intermediate masses.

### III. RESULTS

We first solve the Bethe–Salpeter equation with the potential given in Eq. (4). Employing a cutoff regularization for the loop function  $G$  introduces a parameter  $q_{\max}$ , which sets the momentum-space range of the interaction. As a first step, we adjust  $q_{\max}$  to produce a bound state around 2380 MeV, corresponding to the mass of the  $\Omega(2380)$ . This serves as an initial consistency check of the theoretical framework.

The appearance of a bound state is nontrivial since the diagonal elements of the potential in Eq. (5) vanish. Similarly to the case of  $\Omega(2012)$ , the bound state arises solely due to coupled-channel dynamics. Moreover, the value of  $q_{\max}$  should be physically reasonable, i.e., of the order of the vector-meson mass, as expected for the range of the interaction in momentum space [68, 69].

Fig. 4 shows the modulus squared of the elastic amplitude  $\bar{K}^* \Xi^*$ ,  $|T_{\bar{K}^* \Xi^* \rightarrow \bar{K}^* \Xi^*}|^2$ , for different values of  $q_{\max}$ . Peaks corresponding to bound states are clearly observed in all cases. Based on these results, we select  $q_{\max} = 575$  MeV, which produces a bound-state energy of 2380 MeV. This value is then used in all subsequent calculations.

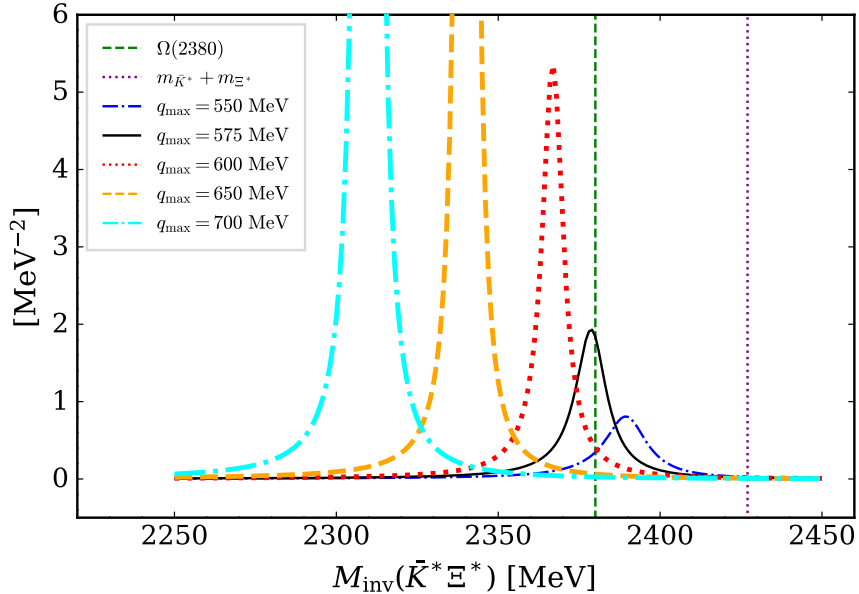


FIG. 4. The modulus squared of the amplitude  $|T_{\bar{K}^* \Xi^* \rightarrow \bar{K}^* \Xi^*}|^2$  for different values of  $q_{\max}$ . The left vertical (green dashed) line corresponds to 2380 MeV, while the right (purple dotted) line indicates the  $\bar{K}^* \Xi^*$  threshold mass.

Fig. 5 shows the modulus squared of the diagonal amplitudes,  $|T_{ii}|^2$ , for the three elastic channels:  $\bar{K}^* \Xi^*$  (channel 1),  $\omega \Omega$  (channel 2), and  $\phi \Omega$  (channel 3). The couplings of the pole to the different channels are defined as [70]

$$|g_i|^2 = \frac{\Gamma}{2} \sqrt{\left| T_{ii}(\sqrt{s} = M_R) \right|^2}, \quad g_j = g_i \frac{T_{ij}(\sqrt{s} = M_R)}{T_{ii}(\sqrt{s} = M_R)}, \quad (57)$$

where  $M_R$  denotes the peak position of  $|T_{ii}|^2$  and  $\Gamma$  its full width at half maximum. The

wave function at the origin, which is relevant for short-range processes, is given by

$$\Psi_i \sim g_i G_i(\sqrt{s} = M_R). \quad (58)$$

The resulting couplings and wave functions at the origin are shown in Table I. The largest value of  $|g_i G_i|$  corresponds to the  $\bar{K}^* \Xi^*$  channel, indicating that this component dominates the structure of the  $\Omega(2380)$  state.

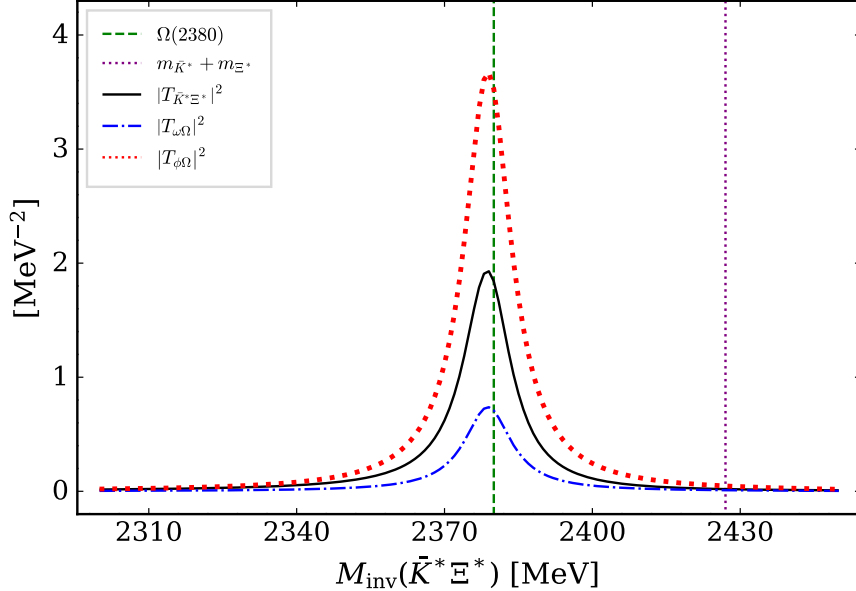


FIG. 5. Modulus squared of the diagonal amplitudes  $|T_{ii}|^2$  for the three channels. The vertical lines have the same meaning as in Fig. 4.

TABLE I. Moduli of the coupling constants ( $|g_i|$ ) and wave functions at the origin ( $g_i G_i$  in MeV) of the three channels.

	$ g_i $	$g_i G_i$
$\bar{K}^* \Xi^*$	2.84	$-27.79 - i2.01$
$\omega \Omega$	2.25	$-18.72$
$\phi \Omega$	3.36	11.31

Next, we include the contributions from the box diagrams shown in Figs. 2 and 3. The coupled-channel space and the real part of the potential  $V_{ij}$  remain unchanged, while the

imaginary parts of the box diagrams are added to the  $\bar{K}^*\Xi^*$  elastic channel,

$$V_{11} \rightarrow V_{11} + i \operatorname{Im} \tilde{V}. \quad (59)$$

We consider three different scenarios: (i) only  $\bar{K}\Xi^*$  box diagrams,  $V_{11} = i \operatorname{Im} \tilde{V}_{\bar{K}\Xi^*}$ ; (ii) only  $\bar{K}^*\Xi$  box diagrams,  $V_{11} = i \operatorname{Im} \tilde{V}_{\bar{K}^*\Xi}$ ; and (iii) the inclusion of both contributions,  $V_{11} = i \operatorname{Im} \tilde{V}_{\bar{K}\Xi^*} + i \operatorname{Im} \tilde{V}_{\bar{K}^*\Xi}$ .

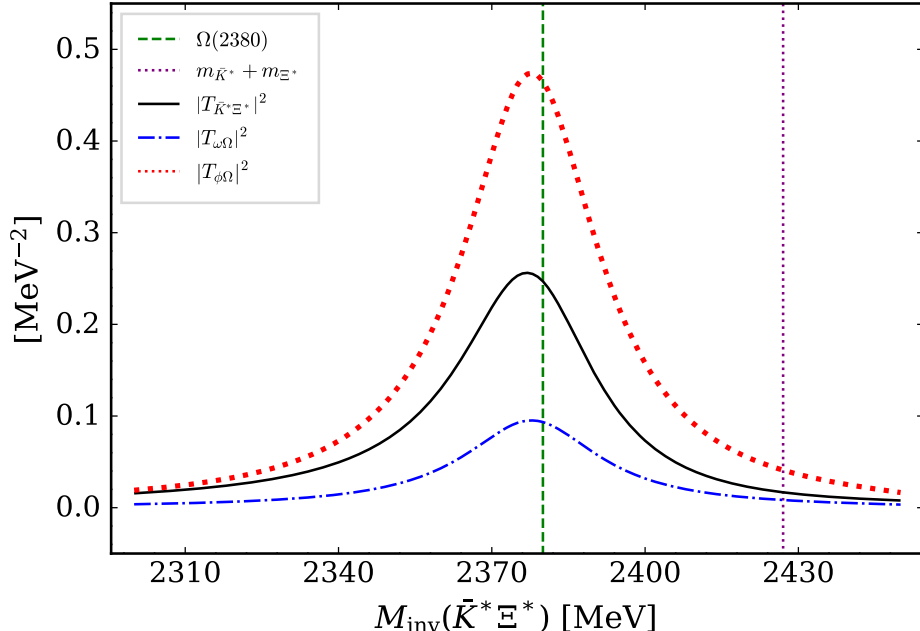


FIG. 6. Same as Fig. 5, but considering the  $\bar{K}\Xi^*$  box diagrams contributions.

From Figs. 6–8, one observes that the peak positions remain close to 2380 MeV in all cases, with small downward shifts of about 2–4 MeV compared to the result without box diagrams shown in Fig. 5. In contrast, the widths increase substantially due to the opening of additional decay channels associated with the box-diagram contributions.

The corresponding couplings and wave functions at the origin ( $g_i G_i$ ) for the three scenarios are collected in Table II. In all cases, the  $\bar{K}^*\Xi^*$  component remains dominant, indicating that the internal structure of the  $\Omega(2380)$  is only weakly affected by the inclusion of the box diagrams. It can be also appreciated that the values of the couplings and the wave functions at the origin do not change appreciably when the box diagrams are taken into account.

Finally, we summarize in the left column of Table III the peak positions and widths for the original case, as well as for the three scenarios including box-diagram contributions. In

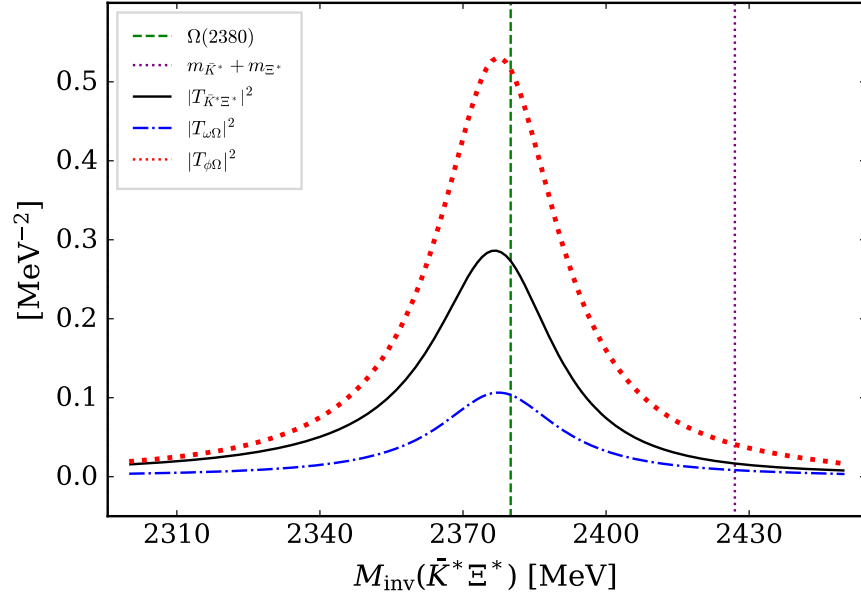


FIG. 7. Same as Fig. 5, but considering the  $\bar{K}^*\Xi$  box diagrams contributions.

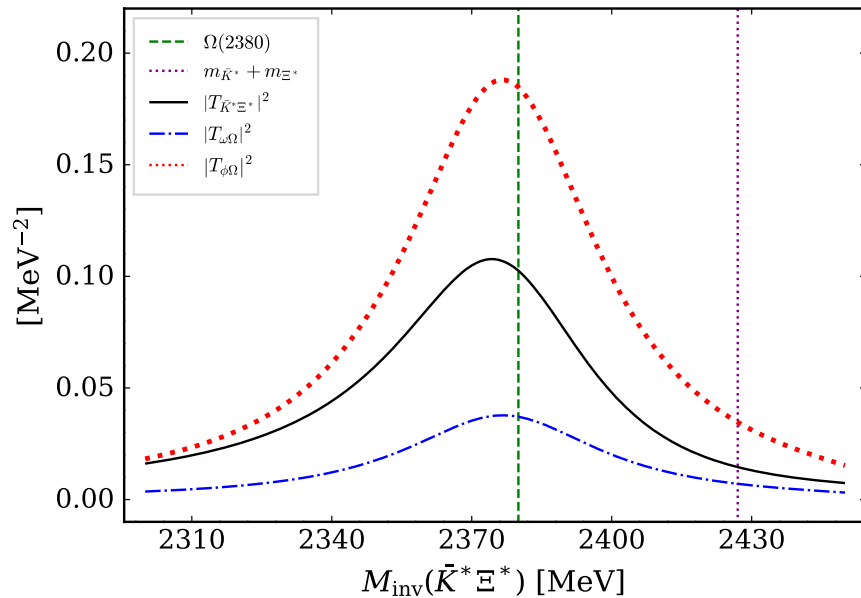


FIG. 8. Same as Fig. 5, but considering the contributions of both kinds of box diagrams.

the original case, the width  $\Gamma_1$  originates solely from the finite widths of the  $\bar{K}^*$  and  $\Xi^*$  particles, which are incorporated through the convolution of the loop functions  $G$  in Eq. (9). For the other three cases, the total widths receive contributions both from this convolution and from the box diagrams.

The  $\bar{K}\Xi^*$  box diagrams correspond to the  $\bar{K}\Xi^*$  decay mode of the  $\Omega(2380)$ , while the

TABLE II. Same results with Table I, but only considering the  $\bar{K}\Xi^*$  box diagrams in the left column, only considering the  $\bar{K}^*\Xi$  box diagrams in the middle column, and considering both box diagrams in the right column.

	$\bar{K}\Xi^*$ box diagrams		$\bar{K}^*\Xi$ box diagrams		both box diagrams	
	$ g_i $	$g_iG_i$	$ g_i $	$g_iG_i$	$ g_i $	$g_iG_i$
$\bar{K}^*\Xi^*$	2.88	$-27.77 - i1.88$	2.84	$-24.45 - i1.88$	2.91	$-27.73 - i1.77$
$\omega\Omega$	2.28	$-18.61 + i2.48$	2.25	$-18.42 + i2.24$	2.26	$-17.92 + i4.61$
$\phi\Omega$	3.40	$11.32 - i1.51$	3.36	$11.20 - i1.36$	3.38	$10.96 - i2.82$

TABLE III. The peak positions and widths of four different cases, without considering any box diagram (the original case), only consider the  $\bar{K}\Xi^*$  box diagrams, only consider the  $\bar{K}^*\Xi$  box diagrams and consider both kinds of box diagrams. The left column corresponds to the results when we take  $\Lambda = 1$  GeV, while for the right one we take  $\Lambda = 800$  MeV. In all cases, the widths of the  $\bar{K}^*$  and  $\Xi^*$  are considered.

	$\Lambda = 1$ GeV		$\Lambda = 800$ MeV	
	peak position	width	peak position	width
Without box diagrams	2379.0 MeV	$\Gamma_1 = 11.6$ MeV	2379.0 MeV	$\Gamma_1 = 11.6$ MeV
Only $\bar{K}\Xi^*$ box diagrams	2376.9 MeV	$\Gamma_2 = 32.5$ MeV	2377.7 MeV	$\Gamma_2 = 26.5$ MeV
Only $\bar{K}^*\Xi$ box diagrams	2377.2 MeV	$\Gamma_3 = 30.0$ MeV	2377.4 MeV	$\Gamma_3 = 27.4$ MeV
Both box diagrams	2375.2 MeV	$\Gamma_4 = 51.5$ MeV	2375.9 MeV	$\Gamma_4 = 42.2$ MeV

$\bar{K}^*\Xi$  box diagrams represent the  $\bar{K}^*\Xi$  decay mode. Including both types of box diagrams effectively accounts for the  $\bar{K}\Xi\pi$  decay channel. Therefore, the partial widths associated with these decay modes can be estimated by subtracting  $\Gamma_1$  from the corresponding total widths,

$$\Gamma_{\bar{K}\Xi^*} = \Gamma_2 - \Gamma_1 = 20.9 \text{ MeV}, \quad (60)$$

$$\Gamma_{\bar{K}^*\Xi} = \Gamma_3 - \Gamma_1 = 18.4 \text{ MeV}, \quad (61)$$

$$\Gamma_{\bar{K}\Xi\pi} = \Gamma_4 - \Gamma_1 = 39.9 \text{ MeV}. \quad (62)$$

From these results we also find the approximate relation  $\Gamma_{\bar{K}\Xi^*} + \Gamma_{\bar{K}^*\Xi} \approx \Gamma_{\bar{K}\Xi\pi}$ , which provides a nontrivial consistency check of our approach. The corresponding branching ratios are then given by

$$\text{Br}[\bar{K}\Xi^*] = \Gamma_{\bar{K}\Xi^*}/\Gamma_{\bar{K}\Xi\pi} = 0.53, \quad (63)$$

$$\text{Br}[\bar{K}^*\Xi] = \Gamma_{\bar{K}^*\Xi}/\Gamma_{\bar{K}\Xi\pi} = 0.47. \quad (64)$$

Comparing these results with those provided by PDG [47], we can appreciate that our results are compatible with the ratio  $\Gamma_{\bar{K}^*\Xi}/\Gamma_{\bar{K}\Xi\pi}$  within the errors. For the case of  $\Gamma_{\bar{K}\Xi^*}/\Gamma_{\bar{K}\Xi\pi}$  we obtain a value of 0.53, which lies close to the upper experimental bound. It would be interesting to have absolute values for this rate in the future, to allow for a better comparison. As for the total width, we obtain  $\Gamma \approx 51.5$  MeV. This should be compared with the experimental width of  $\Gamma_{\text{exp}} = 26 \pm 23$  MeV. Within uncertainties, these values are compatible. This result provides further support for the molecular interpretation of the  $\Omega(2380)$ , since the width depends only weakly on the cutoff  $q_{\text{max}}$ , which is fixed by reproducing the physical mass of the state, and on the parameter  $\Lambda$  associated with the off-shell behavior of the exchanged pion.

To estimate the associated theoretical uncertainties, we repeat the calculation using  $\Lambda = 800$  MeV, a value commonly employed in the literature. The corresponding results are shown in the right column of Table III. In this case, the total width decreases from 51.5 MeV to 42.2 MeV, well within the experimental range. The partial decay widths change moderately, and the resulting branching ratios become

$$\text{Br}[\bar{K}\Xi^*] = 0.48, \quad (65)$$

$$\text{Br}[\bar{K}^*\Xi] = 0.52. \quad (66)$$

As seen from Eqs. (65) and (66), the ratio  $\Gamma_{\bar{K}\Xi^*}/\Gamma_{\bar{K}\Xi\pi}$  becomes smaller than  $\Gamma_{\bar{K}^*\Xi}/\Gamma_{\bar{K}\Xi\pi}$ , in contrast to the previous case, and closer to the experimental bound. Overall, taking into account the theoretical uncertainties, the predicted total width and partial decay widths show a remarkable agreement with the available experimental information.

#### IV. CONCLUSIONS

The discovery of the  $\Omega(2012)$  triggered extensive discussion regarding its nature. Measurements of its decay into  $\bar{K}\Xi$  and  $\bar{K}\pi\Xi$ , together with different theoretical studies, led

the Belle Collaboration to favor a molecular interpretation generated from the  $\bar{K}\Xi^*$  and  $\eta\Omega$  interactions, with  $\bar{K}\Xi$  as a decay channel. It is worth noting that such a state had been predicted prior to its experimental observation [42]. These ideas were subsequently extended to the  $\bar{K}^*\Xi^*$ ,  $\omega\Omega$ , and  $\phi\Omega$  interactions, where a  $J^P = 3/2^-$  resonance was also predicted [48].

In the present work, we identify the  $\Omega(2380)$  as a candidate for this predicted state and extend the approach of Ref. [48] by incorporating the  $\bar{K}\Xi^*$  and  $\bar{K}^*\Xi$  decay channels through box-diagram mechanisms. These contributions provide a sizable enhancement to the width compared to the natural decay of the  $\bar{K}^*\Xi^*$  component. The regulator of the loop functions was fixed to reproduce the mass of the  $\Omega(2380)$ , yielding a cutoff value well within the natural range expected from light vector-meson exchange. The resulting total width, as well as the partial decay widths into the  $\bar{K}\Xi^*$  and  $\bar{K}^*\Xi$  channels, are found to be compatible with the available experimental information.

Overall, our results support the interpretation of the  $\Omega(2380)$  as a dynamically generated resonance arising from vector meson-decuplet baryon interactions. Further experimental and theoretical studies are desirable to validate this picture. In particular, femtoscopic measurements of correlation functions involving the relevant channels—most notably the  $\bar{K}^*\Xi^*$  system—could provide valuable constraints, following dedicated theoretical analyses along the lines of Refs. [71–73] applied to recent ALICE data [74–77]. Alternatively, complementary insight could be obtained through model-independent inverse-amplitude analyses, as proposed in Refs. [78, 79].

## ACKNOWLEDGMENTS

This work is supported by the Spanish Ministerio de Ciencia e Innovación (MICINN) under contracts PID2020-112777GB-I00, PID2023-147458NB-C21 and CEX2023-001292-S; by Generalitat Valenciana under contracts PROMETEO/2020/023 and CIPROM/2023/59. Y.-Y. L. is supported in part by the Guangdong Provincial international exchange program for outstanding young talents of scientific research in 2024. E. O. and A. F. thank the warm support of the ACVJLI.

---

[1] M. Tanabashi *et al.* (Particle Data Group), *Phys. Rev. D* **98**, 030001 (2018).

[2] S. Capstick and N. Isgur, *Phys. Rev. D* **34**, 2809 (1986).

[3] U. Loring, B. C. Metsch, and H. R. Petry, *Eur. Phys. J. A* **10**, 447 (2001), arXiv:hep-ph/0103290.

[4] M. Pervin and W. Roberts, *Phys. Rev. C* **77**, 025202 (2008), arXiv:0709.4000 [nucl-th].

[5] R. N. Faustov and V. O. Galkin, *Phys. Rev. D* **92**, 054005 (2015), arXiv:1507.04530 [hep-ph].

[6] K.-T. Chao, N. Isgur, and G. Karl, *Phys. Rev. D* **23**, 155 (1981).

[7] C. S. Kalman, *Phys. Rev. D* **26**, 2326 (1982).

[8] C. S. An, B. C. Metsch, and B. S. Zou, *Phys. Rev. C* **87**, 065207 (2013), arXiv:1304.6046 [hep-ph].

[9] C. S. An and B. S. Zou, *Phys. Rev. C* **89**, 055209 (2014), arXiv:1403.7897 [hep-ph].

[10] Y. Oh, *Phys. Rev. D* **75**, 074002 (2007), arXiv:hep-ph/0702126.

[11] G. P. Engel, C. B. Lang, D. Mohler, and A. Schäfer (BGR), *Phys. Rev. D* **87**, 074504 (2013), arXiv:1301.4318 [hep-lat].

[12] J. Liang, W. Sun, Y. Chen, W.-F. Qiu, M. Gong, C. Liu, Y.-B. Liu, Z. Liu, J.-P. Ma, and J.-B. Zhang (CLQCD), *Chin. Phys. C* **40**, 041001 (2016), arXiv:1511.04294 [hep-lat].

[13] J. Yelton *et al.* (Belle), *Phys. Rev. Lett.* **121**, 052003 (2018), arXiv:1805.09384 [hep-ex].

[14] S. Jia *et al.* (Belle), *Phys. Rev. D* **100**, 032006 (2019), arXiv:1906.00194 [hep-ex].

[15] S. Jia *et al.* (Belle), *Phys. Lett. B* **860**, 139224 (2025), arXiv:2207.03090 [hep-ex].

[16] M. Ablikim *et al.* (BESIII), *Phys. Rev. Lett.* **134**, 131903 (2025), arXiv:2411.11648 [hep-ex].

[17] S. Acharya *et al.* (ALICE), *Phys. Rev. D* **112**, 092002 (2025), arXiv:2502.18063 [hep-ex].

[18] L.-Y. Xiao and X.-H. Zhong, *Phys. Rev. D* **98**, 034004 (2018), arXiv:1805.11285 [hep-ph].

[19] T. M. Aliev, K. Azizi, Y. Sarac, and H. Sundu, *Phys. Rev. D* **98**, 014031 (2018), arXiv:1806.01626 [hep-ph].

[20] T. M. Aliev, K. Azizi, Y. Sarac, and H. Sundu, *Eur. Phys. J. C* **78**, 894 (2018), arXiv:1807.02145 [hep-ph].

[21] Z.-Y. Wang, L.-C. Gui, Q.-F. Lü, L.-Y. Xiao, and X.-H. Zhong, *Phys. Rev. D* **98**, 114023 (2018), arXiv:1810.08318 [hep-ph].

[22] M. V. Polyakov, H.-D. Son, B.-D. Sun, and A. Tandogan, *Phys. Lett. B* **792**, 315 (2019),

arXiv:1806.04427 [hep-ph].

[23] M.-S. Liu, K.-L. Wang, Q.-F. Lü, and X.-H. Zhong, *Phys. Rev. D* **101**, 016002 (2020), arXiv:1910.10322 [hep-ph].

[24] X. Liu, H. Huang, J. Ping, and D. Chen, *Phys. Rev. C* **103**, 025202 (2021), arXiv:2010.15398 [hep-ph].

[25] A. J. Arifi, D. Suenaga, A. Hosaka, and Y. Oh, *Phys. Rev. D* **105**, 094006 (2022), arXiv:2201.10427 [hep-ph].

[26] H.-H. Zhong, R.-H. Ni, M.-Y. Chen, X.-H. Zhong, and J.-J. Xie, *Chin. Phys. C* **47**, 063104 (2023), arXiv:2209.09398 [hep-ph].

[27] K.-L. Wang, Q.-F. Lü, J.-J. Xie, and X.-H. Zhong, *Phys. Rev. D* **107**, 034015 (2023), arXiv:2203.04458 [hep-ph].

[28] S.-Q. Luo and X. Liu, *Phys. Rev. D* **112**, 014047 (2025), arXiv:2504.14648 [hep-ph].

[29] M. P. Valderrama, *Phys. Rev. D* **98**, 054009 (2018), arXiv:1807.00718 [hep-ph].

[30] Y.-H. Lin and B.-S. Zou, *Phys. Rev. D* **98**, 056013 (2018), arXiv:1807.00997 [hep-ph].

[31] R. Pavao and E. Oset, *Eur. Phys. J. C* **78**, 857 (2018), arXiv:1808.01950 [hep-ph].

[32] Y. Huang, M.-Z. Liu, J.-X. Lu, J.-J. Xie, and L.-S. Geng, *Phys. Rev. D* **98**, 076012 (2018), arXiv:1807.06485 [hep-ph].

[33] T. Gutsche and V. E. Lyubovitskij, *J. Phys. G* **48**, 025001 (2020), arXiv:1912.10894 [hep-ph].

[34] J.-X. Lu, C.-H. Zeng, E. Wang, J.-J. Xie, and L.-S. Geng, *Eur. Phys. J. C* **80**, 361 (2020), arXiv:2003.07588 [hep-ph].

[35] N. Ikeno, G. Toledo, and E. Oset, *Phys. Rev. D* **101**, 094016 (2020), arXiv:2003.07580 [hep-ph].

[36] Y. Lin, Y.-H. Lin, F. Wang, B. Zou, and B.-S. Zou, *Phys. Rev. D* **102**, 074025 (2020), arXiv:1910.13919 [hep-ph].

[37] N. Ikeno, W.-H. Liang, G. Toledo, and E. Oset, *Phys. Rev. D* **106**, 034022 (2022), arXiv:2204.13396 [hep-ph].

[38] Q.-F. Lü, H. Nagahiro, and A. Hosaka, *Phys. Rev. D* **107**, 014025 (2023), arXiv:2212.02783 [hep-ph].

[39] F.-C. Han, Z.-W. Liu, D. B. Leinweber, and A. W. Thomas, *Phys. Rev. D* **112**, L051503 (2025), arXiv:2507.06682 [hep-ph].

[40] Q.-H. Shen, J.-X. Lu, L.-S. Geng, X. Liu, and J.-J. Xie, arXiv preprint (2025), arXiv:2510.13623 [hep-ph].

[41] E. E. Kolomeitsev and M. F. M. Lutz, *Phys. Lett. B* **585**, 243 (2004), [arXiv:nucl-th/0305101](#).

[42] S. Sarkar, E. Oset, and M. J. Vicente Vacas, *Nucl. Phys. A* **750**, 294 (2005), [Erratum: *Nucl.Phys.A* 780, 90–90 (2006)], [arXiv:nucl-th/0407025](#).

[43] S.-Q. Xu, J.-J. Xie, X.-R. Chen, and D.-J. Jia, *Commun. Theor. Phys.* **65**, 53 (2016), [arXiv:1510.07419 \[nucl-th\]](#).

[44] W. L. Wang, F. Huang, Z. Y. Zhang, and F. Liu, *J. Phys. G* **35**, 085003 (2008).

[45] A. Feijoo and I. Vidaña, *Eur. Phys. J. A* **61**, 196 (2025), [arXiv:2411.18248 \[hep-ph\]](#).

[46] D. Gamermann, C. Garcia-Recio, J. Nieves, and L. L. Salcedo, *Phys. Rev. D* **84**, 056017 (2011), [arXiv:1104.2737 \[hep-ph\]](#).

[47] S. Navas *et al.* (Particle Data Group), *Phys. Rev. D* **110**, 030001 (2024).

[48] S. Sarkar, B.-X. Sun, E. Oset, and M. J. Vicente Vacas, *Eur. Phys. J. A* **44**, 431 (2010), [arXiv:0902.3150 \[hep-ph\]](#).

[49] Y. Yan, Y. Wu, Y. Tan, Q. Huang, H. Huang, and J. Ping, arXiv preprint (2026), [arXiv:2601.01338 \[hep-ph\]](#).

[50] M. Bando, T. Kugo, S. Uehara, K. Yamawaki, and T. Yanagida, *Phys. Rev. Lett.* **54**, 1215 (1985).

[51] M. Bando, T. Kugo, and K. Yamawaki, *Phys. Rept.* **164**, 217 (1988).

[52] U. G. Meissner, *Phys. Rept.* **161**, 213 (1988).

[53] H. Nagahiro, L. Roca, A. Hosaka, and E. Oset, *Phys. Rev. D* **79**, 014015 (2009), [arXiv:0809.0943 \[hep-ph\]](#).

[54] V. R. Debastiani, J. M. Dias, W. H. Liang, and E. Oset, *Phys. Rev. D* **97**, 094035 (2018), [arXiv:1710.04231 \[hep-ph\]](#).

[55] W.-F. Wang, A. Feijoo, J. Song, and E. Oset, *Phys. Rev. D* **106**, 116004 (2022), [arXiv:2208.14858 \[hep-ph\]](#).

[56] L. Roca, J. Song, and E. Oset, *Phys. Rev. D* **109**, 094005 (2024), [arXiv:2403.08732 \[hep-ph\]](#).

[57] R. Molina, D. Nicmorus, and E. Oset, *Phys. Rev. D* **78**, 114018 (2008), [arXiv:0809.2233 \[hep-ph\]](#).

[58] L. S. Geng and E. Oset, *Phys. Rev. D* **79**, 074009 (2009), [arXiv:0812.1199 \[hep-ph\]](#).

[59] R. Molina and E. Oset, *Phys. Lett. B* **811**, 135870 (2020), [Erratum: *Phys.Lett.B* 837, 137645 (2023)], [arXiv:2008.11171 \[hep-ph\]](#).

[60] L. R. Dai, R. Molina, and E. Oset, *Phys. Rev. D* **105**, 016029 (2022), [Erratum: *Phys.Rev.D*

106, 099902 (2022)], [arXiv:2110.15270 \[hep-ph\]](https://arxiv.org/abs/2110.15270).

[61] L. R. Dai, E. Oset, A. Feijoo, R. Molina, L. Roca, A. M. Torres, and K. P. Khemchandani, *Phys. Rev. D* **105**, 074017 (2022), [Erratum: Phys.Rev.D 106, 099904 (2022)], [arXiv:2201.04840 \[hep-ph\]](https://arxiv.org/abs/2201.04840).

[62] N. Ikeno, R. Molina, and E. Oset, *Phys. Rev. D* **105**, 014012 (2022), [Erratum: Phys.Rev.D 106, 099905 (2022)], [arXiv:2111.05024 \[hep-ph\]](https://arxiv.org/abs/2111.05024).

[63] A. Bramon, A. Grau, and G. Pancheri, *Phys. Lett. B* **283**, 416 (1992).

[64] Z.-Y. Yang, J. Song, W.-H. Liang, and E. Oset, *Eur. Phys. J. C* **85**, 954 (2025), [arXiv:2412.15731 \[hep-ph\]](https://arxiv.org/abs/2412.15731).

[65] F. E. Close, *An Introduction to Quarks and Partons* (Academic Press, London, 1979).

[66] M. E. Rose, *Elementary Theory of Angular Momentum* (John Wiley & Sons, New York, 1957).

[67] F. Mandl and G. Shaw, *Quantum Field Theory* (John Wiley & Sons, New York, 2010) originally published in 1984.

[68] D. Gamermann, J. Nieves, E. Oset, and E. Ruiz Arriola, *Phys. Rev. D* **81**, 014029 (2010), [arXiv:0911.4407 \[hep-ph\]](https://arxiv.org/abs/0911.4407).

[69] J. Song, L. R. Dai, and E. Oset, *Eur. Phys. J. A* **58**, 133 (2022), [arXiv:2201.04414 \[hep-ph\]](https://arxiv.org/abs/2201.04414).

[70] E. Oset and A. Ramos, *Eur. Phys. J. A* **44**, 445 (2010), [arXiv:0905.0973 \[hep-ph\]](https://arxiv.org/abs/0905.0973).

[71] V. M. Sarti, A. Feijoo, I. Vidaña, A. Ramos, F. Giacosa, T. Hyodo, and Y. Kamiya, *Phys. Rev. D* **110**, L011505 (2024), [arXiv:2309.08756 \[hep-ph\]](https://arxiv.org/abs/2309.08756).

[72] A. Feijoo, M. Korwieser, and L. Fabbietti, *Phys. Rev. D* **111**, 014009 (2025), [arXiv:2407.01128 \[hep-ph\]](https://arxiv.org/abs/2407.01128).

[73] P. Encarnación, A. Feijoo, V. M. Sarti, and A. Ramos, *Phys. Rev. D* **111**, 114013 (2025), [arXiv:2412.20880 \[hep-ph\]](https://arxiv.org/abs/2412.20880).

[74] S. Acharya *et al.* (ALICE), *Eur. Phys. J. C* **83**, 340 (2023), [arXiv:2205.15176 \[nucl-ex\]](https://arxiv.org/abs/2205.15176).

[75] S. Acharya *et al.* (ALICE), *Phys. Lett. B* **845**, 138145 (2023), [arXiv:2305.19093 \[nucl-ex\]](https://arxiv.org/abs/2305.19093).

[76] S. Acharya *et al.* (ALICE), *Phys. Rev. Lett.* **127**, 172301 (2021), [arXiv:2105.05578 \[nucl-ex\]](https://arxiv.org/abs/2105.05578).

[77] I. J. Abualrob *et al.* (ALICE), arXiv preprint (2025), [arXiv:2508.09867 \[nucl-ex\]](https://arxiv.org/abs/2508.09867).

[78] M. Albaladejo, A. Feijoo, I. Vidaña, J. Nieves, and E. Oset, *Eur. Phys. J. A* **61**, 187 (2025), [arXiv:2307.09873 \[hep-ph\]](https://arxiv.org/abs/2307.09873).

[79] A. Feijoo, L. R. Dai, L. M. Abreu, and E. Oset, *Phys. Rev. D* **109**, 016014 (2024), [arXiv:2309.00444 \[hep-ph\]](https://arxiv.org/abs/2309.00444).